Hydrodynamic Performance of a Cycloidal Propulsor in Model-Scale and Full-Scale

Hydrodynamic Performance of a Cycloidal Propulsor in Model-Scale and Full-Scale

Negin Donyavizadeh[1], Alex Shiri[2], Kasper Ljungqvist[2], Arash Eslamdoost[1]

[1]Department of Mechanical Engineering, Chalmers University of Technology, Gothenburg, Sweden

[2]RISE Research Institutes of Sweden, Gothenburg, Sweden

ABSTRACT

A controlled-blade cycloidal propulsion system is an innovative marine propulsor inspired by the dynamic motion of a whale's tail, combining advanced hydrodynamics, smart control, and sustainable design in one system, with a unique feature of blade rotation and pitching via a trajectory function. In this study, the effect of scale on the hydrodynamic performance of a cycloidal propulsor with a trajectory function is evaluated in open-water conditions. For this purpose, a three-dimensional geometry consisting of a rotating disk with vertical blades that have pitching motions is numerically simulated through unsteady Reynolds-averaged Navier-Stokes (RANS) and k-ω SST turbulence model to predict hydrodynamic performance. The trajectory function defines the prescribed pitching motion of each blade during one orbital cycle. This function remains fixed and is not influenced by the surrounding flow field. However, its hydrodynamic effects differ considerably between model-scale and full-scale conditions. Variations of Reynolds number in model-scale and full-scale during one complete orbit are investigated. Differences in Reynolds numbers across the two scales lead to variations in viscous and unsteady flow behaviors, which in turn influence the overall thrust and torque trends. The current research compares the performance of the cycloidal propulsor in model-scale and in full-scale through analysing the open-water curves as well as pressure and shear force variations across these scales.

Keywords

Controlled-blade cycloidal propeller, Hydrodynamic performance, Trajectory function, Open-Water characteristics.

1 INTRODUCTION

The marine transport industry is currently pursuing the development of propulsion systems that aim to achieve better maneuverability, lower environmental impact, and high efficiency. Also, to reduce emissions of environmental pollutants, in line with international regulations, and to address increasing energy costs, various studies are being conducted to find a suitable solution to replace conventional propulsion systems.

Conventional propulsion systems have a long history of use. These systems face limitations in terms of efficiency and maneuverability in various operating conditions. However, the cycloidal propulsion system offers different types of characteristics than conventional propellers, and that's why there is an interest to study. This system consists of a horizontal rotating disk with vertical fins mounted on it, each fin having the ability to change the pitch angle during its orbital motion by the trajectory function, so that the angle of attack against the incoming flow changes continuously, which determines the unique hydrodynamic properties of cycloidal propellers. This system can produce thrust in different directions instantaneously, and as a result, it increases the controllability and maneuverability of the vessel. Numerous theoretical, experimental, and numerical studies have investigated their performance in terms of efficiency, thrust, and torque. Brockett et al. (1991) studied the performance and three-dimensional flow around cycloidal propellers using a lifting-line model combined with an actuator-disk model to predict the hydrodynamic loads on a cycloidal propeller. Each fin of the cycloidal propeller, at a given angular position, was represented by using a lifting-line type model. Its local hydrodynamic loads were calculated from sectional lift and drag relations with a quasi-steady assumption. In addition, an actuator disk model was used to provide the induced velocity generated by all blades, which was used as the input lifting-line model. The low-order model was a physics-based analytical formulation combining thin airfoil theory and nonlinear lifting-line correction to predict instantaneous forces on the blades without resolving the full Navier-Stokes equations. It was shown that the numerical method was suitable for initial design and that some modifications to fin pitch control could increase thrust with little change in efficiency (Brockett et al. 1991).

In recent years, increasing demands for highly maneuverable and efficient propulsion systems have motivated the investigation and improvement of the analytical modeling methods. A low-order unsteady hydrodynamic model for a cycloidal propeller was presented and validated by in-house experiments. The model considers the effects of dynamic virtual camber, leading-edge vortices, and near and shed wakes, and the results are in good agreement with experimental data at low Reynolds numbers (Halder et al. 2018).

In cycloidal propellers, the motion of the blade in a curved and unsteady flow field causes a chord-wise variation of flow incidence, and a symmetric blade behaves like a cambered airfoil, which is called dynamic virtual camber. A rapid pitching angle is really important and crucial in increasing hydrodynamic forces, especially at higher Reynolds numbers. Because it can affect the separation of the flow at the leading edge and the formation of the leading-edge vortex, this unsteady motion of the fins also affects the vorticities downstream, and part of that is called the near wake of the blade, which directly affects the blade loads through induced velocities.

A five-bladed cycloidal propeller with a NACA 0012 profile with a simplified two-dimensional model was studied by Hu et al. (2020). In this study, the results showed that the position of the fin center of rotation and operating conditions have a significant impact on the propeller's power, torque, and efficiency.

Sun et al. studied the hydrodynamic performance of a three-blade propeller with a flap at the trailing edge by using CFD (Sun et al. 2021). Three flap motion patterns (anti-virtual camber, sinusoidal, and combined) were investigated. The results showed that anti-virtual camber motion reduces lateral thrust and sinusoidal motion increases efficiency, and their combination produces both effects simultaneously. They also investigated the flow mechanism and the effect of the flap on the propeller performance.

Hu et al. (2022) investigated the transient four-quadrant hydrodynamics of a 3D half-blade of cycloidal propellers. So, half of the computational domain was simulated, and the symmetry boundary condition was applied. The results showed that changing the azimuth angle significantly affects the hydrodynamic loads and the direction of the ship's movement, and the non-uniform flow increases the unwanted side forces.

Halder et al. (2024) investigated an unsteady hydrodynamic model for a cycloidal propeller in translational motion. They simulated the effect of motion speed on flow. As the advance ratio increases, the side force increases, and the propulsive force decreases, and at high advance ratios, the blade experiences negative tangential force and extracts energy from the flow.

Labasse et al. (2023), using overlapping mesh methods (Chimera) and the OpenFOAM tools, define that theoretical thrust-scaling laws can be matched with time-averaged numerical results, even in nonlinear motion conditions. It has also been found that these thrust prediction laws remain valid for pitching-rotating motions such as cycloidal propeller blades, and the mean pressure correction induced by the additional surging motion is relatively small.

Liu et al. (2024) investigated and reviewed the different studies of the Voith–Schneider propeller. In this review paper, the nonlinear hydrodynamic behavior of this propulsion system and results from the coupling of uniform rotational motion and variable blade rotation were studied. They obtained that controlling the trajectory curve and asymmetric distribution of blade rotation angle can significantly improve the efficiency, so that in the six-blade configuration, an efficiency increase is obtained.

Unlike conventional cycloidal propellers that use a mechanical steering system to vary the blade pitch, new approaches focus on independent and electrical control of the blades, which allows for the investigation of more complex fin trajectories (Fasse et al. 2024).

In this paper, the ABB Dynafin™ propeller, introduced by ABB, is considered a new generation of cycloidal propellers. The ABB Dynafin™ consists of a large horizontal wheel, driven by an electric motor at a relatively low speed (around 30 to 80 rpm), with five vertical fins mounted on the wheel, each controlled by a separate motor. This paper aims to numerically evaluate the hydrodynamic performance of the ABB Dynafin™ at a full-scale and model-scale to figure out the different behaviours in the flow physics across these scales and compare the open-water performance. A geometry of a cycloidal propeller with five vertical fins with orbital and pitching motion is simulated using three-dimensional unsteady RANS equations with the k-ω SST turbulence model. The performance parameters, including thrust, torque, and power, are predicted. The numerical results are compared with the experimental data from open-water tests. Apart from these global quantities, the forces acting on one individual fin are also investigated.

2 NUMERICAL METHOD

In this study, Computational Fluid Dynamics (CFD) has been used to evaluate the performance of the cycloidal propulsor in full-scale and model-scale. The computations are carried out utilizing the Reynolds-Averaged Navier-Stokes (RANS) approach in STAR-CCM+ (version 2502). To discretize the continuous equations and solve the conservation equations for mass, momentum, and turbulence, a finite volume method is used, considering a second-order spatial discretization scheme and a segregated approach for coupling velocity and pressure fields. Time integration is performed using a second-order implicit temporal discretization scheme.

Turbulence is modelled using the Shear Stress Transport (SST k-ω) turbulence model. The Rigid Body Motion (RBM) method is employed for simulating the motions of the fins and the main wheel. The RBM approach is commonly referred to as the sliding mesh technique.

2.1 GEOMETRY AND MOTION OF THE CYCLOIDAL PROPELLER

To achieve the goals of this study, it is crucial to understand how the cycloidal propeller's fins rotate and pitch. Therefore, in this section, the geometry and the pitching function of the cycloidal propeller are introduced.

The schematic of a cycloidal propeller, including five fins and a rotating wheel, is shown in Figure 1.

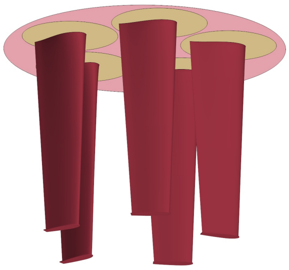

Figure 1: Schematic of the cycloidal propeller

This geometry has been used to study the hydrodynamic characteristics of the cycloidal propeller in the full-scale and model-scale, with a scale factor of 13.37. The main geometrical specifications of the propeller at full-scale and model-scale are presented respectively, in Table 1.

Table 1: Specification of the cycloidal propeller geometry at full-scale (FS) and model-scale (MS)

Symbol	FS	MS	Definition
N	5	5	Number of Fins (-)
D	5	0.3739	Propeller Diameter (m)
d	3	0.2243	Orbital Diameter (m)
C	0.85	0.0636	Fin chord length (m)
S	3.5	0.2617	Fin Span Length (m)

The cycloidal propeller consists of a main wheel with a diameter of D (propeller diameter, m), driven by a main motor rotating at a constant speed of n (main wheel rotational speed, rps). Five pitching fins are mounted on the main wheel, with their pivot points located on a circle with a diameter of d (orbital diameter, m). Each of these fins individually oscillate with an angular velocity of ω (fin rotational speed, radps) around its own pivot point while rotating in orbit on the main wheel. The ratio of the inflow velocity V_a to the peripheral velocity of the fin $u = \pi.d.n$, is called an advance ratio (λ) which is shown in Equation (1):

$$\lambda = \frac{V_a}{u} = \frac{V_a}{\pi.d.n} \tag{1}$$

Each fin's trajectory is prescribed by the combined motion of the rotational speed of the main wheel, as well as the oscillations of each fin around its pivot point.In this study, λ is 1.25. If λ is less than 1, the trajectory of a fin is in a trochoidal mode, which is shown in Figure 2 with a variable instantaneous angle of attack.

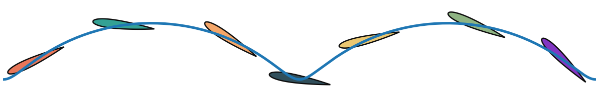

Figure 2: Trochoidal path of one fin

2.2 COMPUTATIONAL DOMAIN

To capture the flow around the cycloidal propeller, a cubic computational domain is used. The computational domain size is shown in Figure 3.

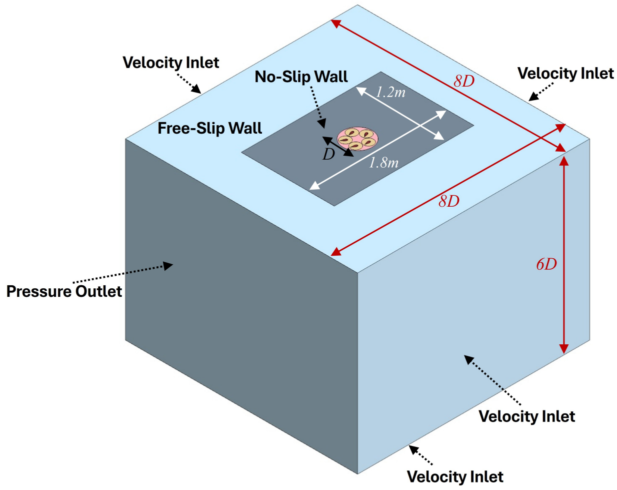

Figure 3: Computational Domain

The computational domain consists of one cube to simulate the far field flow, a large cylindrical sub-domain that surrounds the propulsor and rotates at a fixed speed (n), and six smaller cylindrical sub-domains around each fin, to implement the oscillation of the fins. These sub-domains are connected using interfaces. A top view of these sub-domains is shown in Figure 4.

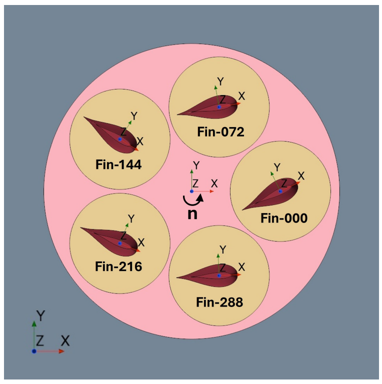

Figure 4: The rotating sub-domains and coordinate systems

So, the computational domain is divided into seven parts: five rotating cylindrical regions around the fins, which rotate around their own local coordinate system, one larger rotating cylinder including the five rotating cylinders, which rotates around the global coordinate system, and a large cubic region, including the top mount plate.

The boundary conditions that are applied on the computational domain are shown in Figure 3. No-slip boundary condition is used on all the fins, on the rotating and pitching plates on the top of the unit, as well as the top mount plate (all surfaces shown in Figure 4). A uniform velocity inlet boundary condition is assigned to all the boundaries marked with velocity inlet in Figure 3. In this study, the main focus is on one advance ratio, which is the design point. In the cycloidal propeller, for each advance ratio, there is an individual trajectory function that is designed to obtain maximum efficiency. So, in this case study, for the current trajectory function, the design point is the advance ratio, which is explained below. The inlet velocity in the full-scale simulation is 9.26 m/s, and in the model-scale simulation, the inlet velocity is 2.5323 m/s to satisfy the same advance ratio (λ). Therefore, the main wheel rotational speeds (n) in full-scale and model-scale are 47.1313 (rpm) and 172.3236 (rpm), respectively. The outlet boundary in this figure is assigned to be a pressure outlet boundary condition.

2.3 GRID GENERATION

To discretize the computational domain, an unstructured trimmed mesh is employed for the fixed region of the computational domain (the cubic domain). An unstructured polyhedral mesh is utilized for the rotating cylindrical regions.

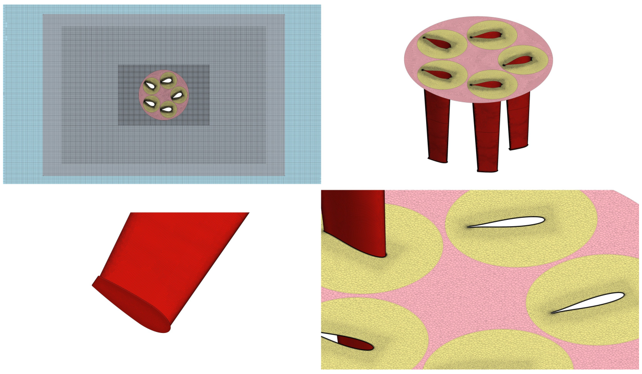

Figure 5: Overview of the grids near the cycloidal propulsor in full-scale

To ensure that the mesh in the full-scale and model-scale have a similar distribution in the far-field, the sizes of unstructuredmeshes outside the boundary layer is scaled using the geometrical scale factor, 13.37. The stretch factor for prism layer meshes at full-scale and model-scale is set to 1.339. Due to the different Reynolds numbers between these scales, the prism layer thickness and the number of layers inside the prism layers vary. In model scale, the first cell height is adjusted to guarantee $y^+ = 1$ over the fins, which allows us to resolve the boundary layer down to the wall. However, keeping the same prism layer refinement in full-scale can lead to a substantial increase in the total number of cells. Therefore, a coarser prism layer mesh is used in full-scale to reduce the computational cost. With this prism layer in full-scale, y^+ varies between values around 1 to 150. Consequently, the all y^+ wall treatment approach is used in full-scale. This approach switches between wall-function and wall-resolved treatment depending on the local y^+ value. The number of prism layers on the fin's surface is set to 24 layers at full-scale and 12 layers at model-scale. In full-scale and model-scale, these settings lead to 42900528 cells and 22101246 for the entire computational domain, respectively. In full-scale, the mesh is divided into several regions: 15509211 cells in the fixed domain, 1721307 cells in the larger rotating cylindrical domain, and 5134002 cells in each of the small rotating cylinders. The grid in full-scale, on the computational domain, fins, end plate, and in the middle of the fin span are shown in Figure 5.

2.4 COMPUTATIONAL TIME STEP

In the current simulations, the computational time step is determined based on the rotational speed of the cycloidal propeller in the Global Coordinate System. The time step is set to correspond to one degree rotation of the main wheel. The rotational speeds in full-scale and model-scale are 47.1313 (rpm) and 172.3236 (rpm), respectively, which leads to respective time steps of 3.54×10^{-3} and 9.67×10^{-4} s.

2.5 HYDRODYNAMIC COEFFICIENTS

To compare the results of full-scale simulation with model-scale simulation, non-dimensional coefficients are defined.

Thrust coefficient K_T, torque coefficient K_Q, power coefficient K_P and efficiency η are defined as follows:

$$K_T = \frac{T}{\rho n^2 d^3 S} \tag{2}$$

$$K_Q = \frac{Q}{\rho n^2 d^4 S} \tag{3}$$

$$K_P = \frac{Power}{\rho n^3 d^4 S} \tag{4}$$

$$\eta = \frac{V_a T}{Power} \tag{5}$$

where, T is the thrust in the direction of advance velocity V_a, Q is the effective torque of the wheel and fins. Due to the different pivot axis of the wheel and fins, it is calculated from the total power as $Q = Power/2\pi n$. d is the orbital diameter, S is the fin span and n is the rotational speed of wheel in rps.

3 RESULTS AND DISCUSSION

In this section, the results of numerical simulation for both full-scale and model-scale are compared. However, before discussing the scale effects, a comparison of the computed and measured model-scale open-water performance is presented in this section. The open-water experimental tests of the cycloidal propulsor were carried out in RISE's towing tank at SSPA Maritime Center, which is 260 m long, 10 m wide, and 5 m deep (Donyavizadeh et al. 2026). The open-water tests were conducted at a speed of 2.528m/s corresponding to the advance ratio of $\lambda = 1.25$. Each test run was performed at 15-minute intervals to ensure that the eddies in the basin remained minimal. Throughout the open-water tests, stationary measurements at zero speed were periodically performed to verify the consistency of the signals. Calibration tests without mounted fins were carried out in order to get correction values for the torque and thrust of the system. The comparison between the CFD and EFD results is made at an advance ratio of λ=1.25 and upstream velocity of 2.5323 m/s.

Before comparing the computed and measured performance of the cycloidal propulsor, it is essential to verify that the behavior of the fins across a full orbit in the experiments and the simulations are the same. This is achieved through comparing the pitch angle γ (rad) and the angular velocity of ω (radps) of one fin, for both CFD and EFD. Figure 6 depicts the pitch angle of one fin over one revolution of the unit. The X-axis shows the rotational angle of the wheel (θ), and the Y-axis shows the pitch angle of one fin (γ) in radians.

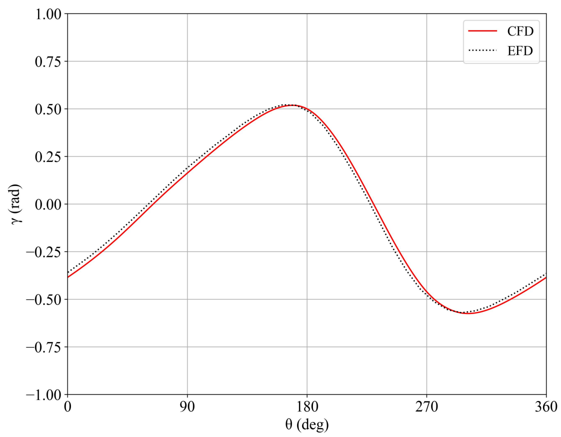

Figure 6: Pitching angle of one fin over a wheel cycle in EFD and CFD at model-scale (λ=1.25)

Moreover, Figure 7 shows the angular velocity of one fin over one revolution of the unit. The X-axis shows the rotational angle of the wheel (θ), and the Y-axis shows the angular velocity of the fin (ω) in radian per second.

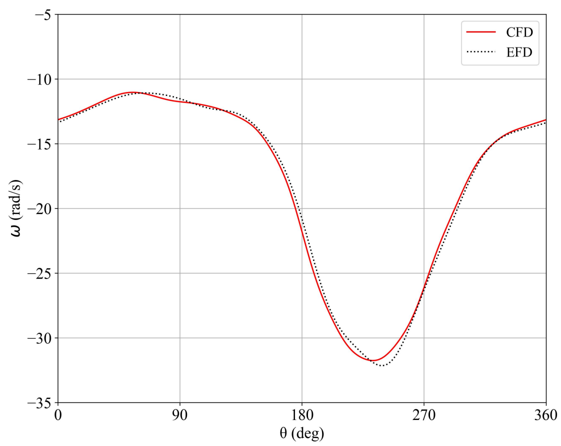

Figure 7: Rotational speed of one fin over a wheel cycle at in EFD and CFD model-scale (λ=1.25)

The time-averaged values of thrust (T), torque (Q), and efficiency (η), and also the comparative differences, are shown in Table 2. Overall, the numerical results show a good agreement with experimental data, exhibiting small relative errors for all evaluated performance parameters. A more detailed comparison of the CFD and EFD results can be found in Donyavizadeh et al. (2026).

Table 2: Time-averaged EFD and CFD results at model-scale and their relative differences (λ=1.25)

	EFD	CFD	$\Delta\%$
T (N)	65.22	67.53	3.54
Q (N·m)	13.20	13.42	1.66
K_P (-)	15.21	15.46	1.66
K_T (-)	2.68	2.78	3.54
K_Q (-)	2.42	2.46	1.66
η (%)	69.32	70.60	1.85

After validating the numerical simulations, the results of the full-scale and model-scale simulations are investigated and compared. Table 3 shows the computed non-dimensional hydrodynamic coefficients of K_T, K_Q, and η at λ=1.25 (V_a=9.26 m/s in full-scale and V_a=2.5323 m/s in model-scale).

Table 3: Time-averaged hydrodynamic coefficients at full-scale and model-scale as well as their relative differences (λ=1.25)

	FS	MS	$\Delta\%$
K_P (-)	14.85	15.63	5.25
K_T (-)	2.92	2.77	5.12
K_Q (-)	2.36	2.49	5.25
η (%)	77.23	69.65	9.82

Besides the time-averaged results, analysing the time history of the hydrodynamic coefficients over one wheel revolution provides additional insight. Figure 8 shows the time history of the thrust coefficient at full-scale and model-scale for λ=1.25. The results show that the full-scale K_T is consistently larger than corresponding model-scale value throughout the wheel revolution.

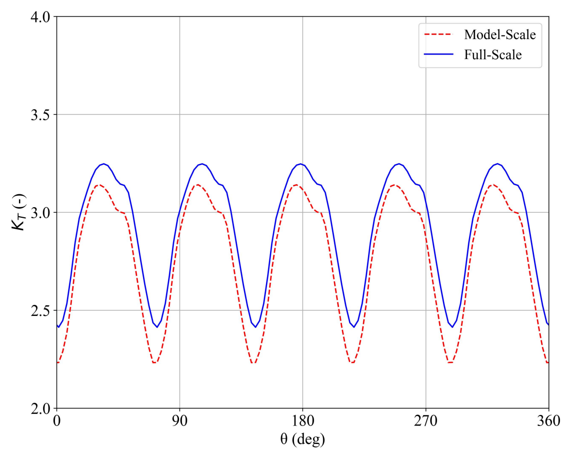

Figure 8: Variation of thrust coefficient over a wheel cycle at full-scale and model-scale (λ=1.25)

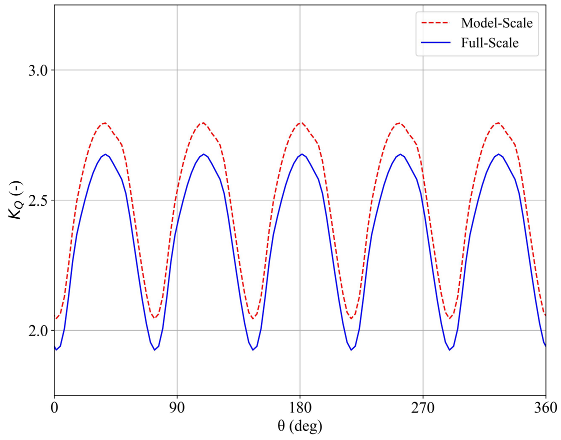

Figure 9: Variation of torque coefficient over a wheel cycle at full-scale and model-scale (λ=1.25)

The variation of torque coefficient over a wheel cycle at at full-scale and model-scale are shown in Figure 9 for λ=1.25. As can be seen in this figure, in contrast to K_T, the value of K_Q at the full-scale is smaller than the corresponding value at model-scale over the entire wheel revolution. However, the discrepancies are more pronounced around the peaks and valleys of K_Q.

By comparing the maximum value of K_T and K_Q time-histories to the mean values, it can be obtained that the variation of the signals of K_T over time, for full-scale, is 11.28% and for model-scale is 13.41%. Also, the variation of the signals of K_Q over time, for full-scale, is 13.25% and for model-scale is 12.42%.

The power coefficient K_P at both scales in λ=1.25 is shown in Figure 10. The amplitude of the oscillation of K_P over a full wheel cycle is 13.25% of its mean value at full-scale and 12.42% of its mean value at model-scale.

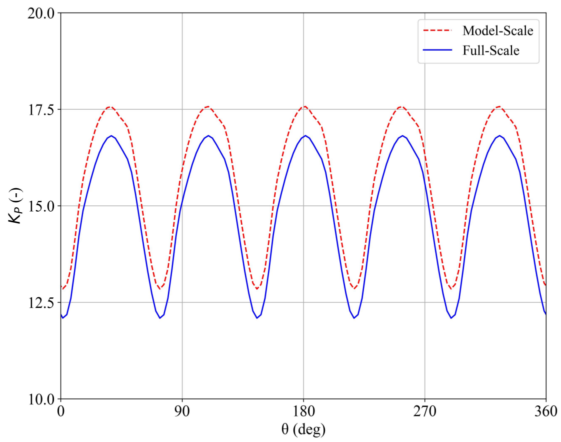

Figure 10: Variation of power coefficient over a wheel cycle at full-scale and model-scale (λ=1.25)

The hydrodynamic efficiency at full-scale and model-scale for λ=1.25 is shown in Figure 11.

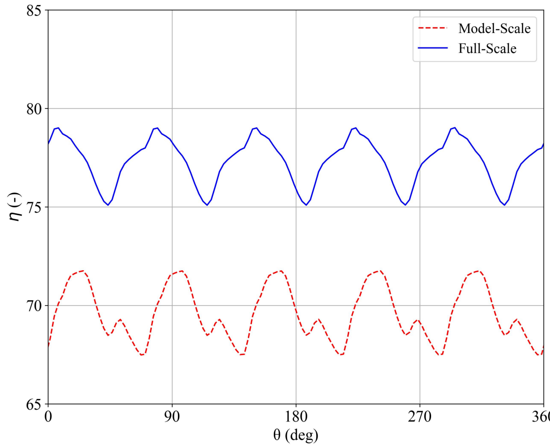

Figure 11: Variation of hydrodynamic efficiency over a wheel cycle at full-scale and model-scale (λ=1.25)

As seen in this figure, the hydrodynamic efficiency in full-scale is significantly larger (in average more than 9.45%) in comparison to the efficiency at model-scale. This is mostly due to higher Reynolds number and thus reduced viscous effects at full-scale in comparison to model-scale. Furthermore, the variation of the instantaneous hydrodynamic efficiency about its mean value over one wheel revolution is reduced at full-scale compared with model-scale, resulting in more stable efficiency characteristics.

To shed more light into the differences between model-scale and full-scale performances, the time-histories of the force and moment acting on a single blade are also studied. Moreover, the pressure and shear components of these force and moments are extracted and compared across these scales. Here, the hydrodynamic forces in the x-direction (opposite to the upstream flow direction), represent thrust, and the moment about the z-axis, represents torque exerted on a single fin.

The Non-dimensional form of the pressure component $(K_{T_p})_{fin}$ and shear force component $(K_{T_s})_{fin}$ are used to facilitate a more meaningful comparison between these scales. Similarly, the fin torque coefficient is decomposed into pressure and shear components, $(K_{Q_p})_{fin}$ and $(K_{Q_s})_{fin}$.

This decomposition is performed because the pressure and shear force components arise from different physical mechanisms and exhibit distinct Reynolds-number dependencies, leading to different behaviour at model and full scales. The shear stress is directly influenced by Reynolds number. In an ideal flow (inviscid and irrotational flow) the normalized pressure is not influenced by Reynolds number variation. However, in a viscous flow, the growth of boundary layer over a solid surfaces leads to departure from this assumption due to viscous pressure term. The goal of decomposing force and moment into its pressure and shear components is to figure out the Reynolds number dependency of the flow is a more detailed approach.

To better analyze the pressure and shear force coefficients and compare them, the right position of a fin and the apparent angle of attack of it during the wheel revolution is shown in Figure12.

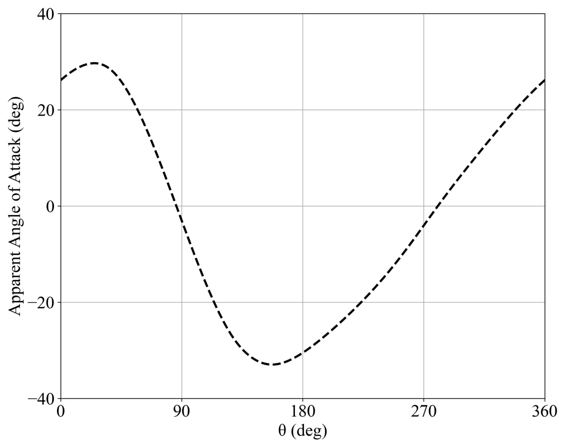

Figure 12: Apparent angle of attack of a fin over one wheel cycle

Figure 13 shows the contribution of pressure forces to the variation of thrust coefficient $(K_{T_p})_{fin}$ of a single fin throughout one full wheel cycle at full-scale and model-scale for λ=1.25. This figure reveals that the pressure forces are quite similar at both scales. The pressure component of the thrust coefficient at these scales slightly deviate from each other when θ is around $45°$ and $180°$. As seen in Figure12, at these fin positions the apparent angle of attack is at its maximum (close to $\pm 30°$), which leads to a thicker boundary layer over the blade and thus stronger viscous pressure contribution.

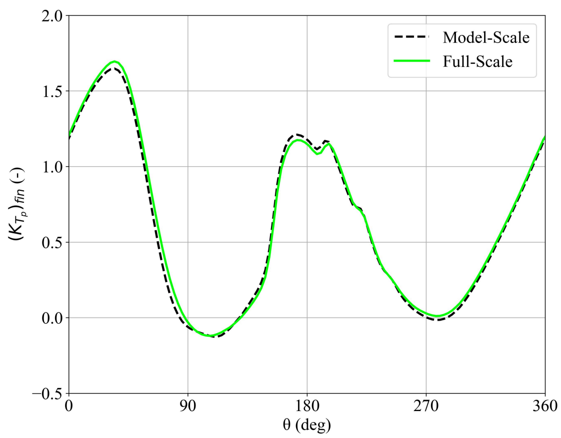

Figure 13: Variation of pressure component of thrust coefficient of a single fin over a wheel cycle at full-scale and model-scale (λ=1.25)

The contribution of shear stress to the variation of thrust coefficient $(K_{T_s})_{fin}$ of a single fin throughout one full wheel cycle is shown in Figure 14. Unlike the $(K_{T_p})_{fin}$ trends in Figure 13, the $(K_{T_s})_{fin}$ at full-scale and model-scale show a different behavior. As can be seen in Figure 14, the amplitude of model-scale $(K_{T_s})_{fin}$ is clearly larger than the full-scale value. The comparison between the $(K_{T_p})_{fin}$ and the $(K_{T_s})_{fin}$, shows that the thrust is primarily dominated by the pressure component while the shear force contribution is significantly smaller.

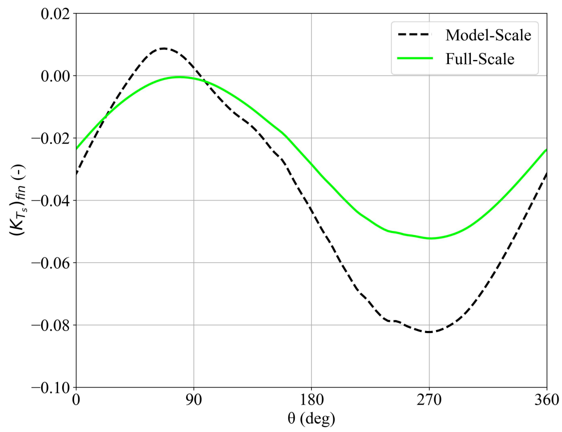

Figure 14: Variation of shear component of thrust coefficient on a single fine over a wheel cycle at full-scale and model-scale (λ=1.25)

A single blade torque is obtained around its pivot point. Figure 15 shows the variation of pressure component of the torque coefficient for a single fin $(K_{Q_p})_{fin}$ over a wheel cycle at at full-scale and model-scale for λ=1.25. The $(K_{Q_p})_{fin}$ at full-scale and the model-scale have the same overall trends, but around θ $45°$ and $315°$, the differences between the full-scale and the model-scale become larger.

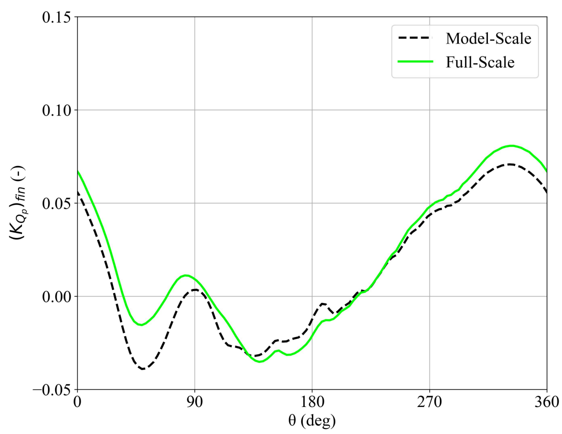

Figure 15: Variation of pressure component of torque coefficient of a single fin over a wheel cycle at full-scale and model-scale (λ=1.25)

The shear stress component of torque coefficient of a single foil at full-scale and model-scale for λ=1.25 is shown in Figure 16. As seen in this figure, this component of the torque coefficient is about two orders of magnitude smaller than the pressure component. For most of the fin positions through out the wheel cycle, the $(K_{Q_s})_{fin}$ at full-scale has a larger value than the value at model-scale.

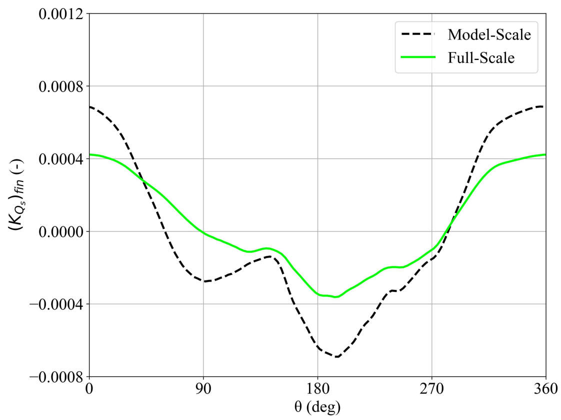

Figure 16: Variation of shear component of torque coefficient of a single fin over a wheel cycle at full-scale and model-scale (λ=1.25)

Overall, the results show that scale effects have a significant impact on hydrodynamic performance. While the pressure component dominates at both scales, the shear force effects are more sensitive to scale differences between model-scale and full-scale. This highlights the importance of considering the effect of Reynolds number in generalizing the results to full-scale.

4 CONCLUSION

In this study, the hydrodynamic performance of the cycloidal propeller at model-scale and full-scale is investigated using 3D unsteady simulation (URANS with SST k-ω turbulence model).

Firstly, the numerical results were validated with experimental data from an open-water test conducted in a towing tank at model-scale. The comparison between the time-averaged thrust, torque, and efficiency obtained from experimental data and numerical results shows a good agreement.

The comparison of the average non-dimensional hydrodynamic coefficients for the whole unit at λ=1.25 shows that at full-scale, the time-averaged K_T is larger than the corresponding model-scale values, while the time-averaged K_Q is smaller. This leads to an increased efficiency η at full-scale.

Decomposing thrust and torque into their pressure and shear stress components shows that the pressure contribution is dominant at both scales and its trend remains almost independent of Reynolds number, but the shear stress contribution has a larger amplitude at the model-scale, which is due to stronger viscous effects at lower Reynolds numbers.

ACKNOWLEDGEMENTS

This work has been funded by the Swedish Transport Administration (Trafikverket). The experimental measurements are carried out at RISE - SSPA Maritime Center.

We acknowledge the National Academic Infrastructure for Supercomputing in Sweden (NAISS), partially funded by the Swedish Research Council through grant agreement no. 2022-06725.

The data handling was enabled by resources provided by the National Academic Infrastructure for Supercomputing in Sweden (NAISS), partially funded by the Swedish Research Council through grant agreement no. 2025-23605.

REFERENCES

Brockett, T. (1991). 'Hydrodynamic analysis of cycloidal propulsors'. SNAME 6th Propeller and Shafting Symposium, Virginia, USA.

Donyavizadeh, N., Shiri, A., Ljungqvist, K., Långström, A. & Eslamdoost, A. (2026).'Numerical and experimental evaluation of the open-water performance of a cycloidal propeller'. OMAE2026, Tokyo, Japan.

Fasse, G., Becker, F., Hauville, F., Astolfi, J. A. & Germain, G. (2022). 'An experimental blade-controlled platform for the design of smart cross-flow propeller'. Ocean Engineering **250**, pp. 110921.

Fasse, G., Sacher, M., Hauville, F., Astolfi, J. A. & Germain, G. (2024). 'Multi-objective optimization of cycloidal blade-controlled propeller: An experimental approach'. Ocean Engineering **299**, pp. 117363.

Halder, A., Heimerl, J. & Benedict, M. (2024). 'Hydrodynamic modeling and experimental validation of cycloidal propeller in translational motion'. Ocean Engineering **295**, pp. 116826.

Halder, A., Walther, C. & Benedict, M. (2018). 'Hydrodynamic modeling and experimental validation of a cycloidal propeller'. Ocean Engineering **154**, pp. 94105.

Hu, J., Li, T. & Guo, C. (2020). 'Two-dimensional simulation of the hydrodynamic performance of a cycloidal propeller'. Ocean Engineering **217**, pp. 107819.

Hu, J., Yan, Q., Ding, J. & Sun, S. (2022). 'Numerical study on transient four-quadrant hydrodynamic performance of cycloidal propellers'. Engineering Applications of Computational Fluid Mechanics **16.1**, pp. 1813– 1832.

Labasse, J., Ehrenstein, U., Fasse, G. & Hauville, F. (2023). 'Thrust scaling for a large-amplitude heaving and pitching foil with application to cycloidal propulsion'. Ocean Engineering **275**, pp. 114169.

Liu, W., Liu, Z., Chen, Q. & Ma, C. (2024). 'Research on efficiency optimization of the Voith-Schneider propeller based on motion curve parameter control'. Ocean Engineering **299**, pp. 117136.

Sun, Z., Li, H., Liu, Z. H., Wang, W. Q., Zhang, G. Y., Zong, Z. & Jiang, Y. C. (2021). 'Study on hydrodynamic performance of cycloidal propeller with flap at the trailing edge'. Ocean Engineering **237**, pp. 1068657.